AGU PUBLICATIONS

JGR

Journal of Geophysical Research: Space Physics

RESEARCH ARTICLE

10.1002/2014JA020401

Special Section:
Low-Frequency Waves in Space Plasmas

The effect of magnetopause motion on fast mode resonance

M. D. Hartinger[1], D. Welling[1], N. M. Viall[2], M. B. Moldwin[1], and A. Ridley[1]

[1]Department of Atmospheric, Oceanic, and Space Sciences, University of Michigan, Ann Arbor, Michigan, USA, [2]NASA Goddard Space Flight Center, Greenbelt, Maryland, USA

Key Points:
- Typical magnetopause motion does not affect fast mode resonance occurrence
- Magnetopause motion cannot explain why FMR is rarely observed
- Selection criteria and non-FMR wave activity affect FMR occurrence rate

Supporting Information:
- Readme
- Figure S1
- Figure S2
- Figure S3

Correspondence to:
M. D. Hartinger,
mdhartin@umich.edu

Citation:
Hartinger, M. D., D. Welling, N. M. Viall, M. B. Moldwin, and A. Ridley (2014), The effect of magnetopause motion on fast mode resonance, *J. Geophys. Res. Space Physics*, *119*, 8212–8227, doi:10.1002/2014JA020401.

Received 17 JUL 2014
Accepted 18 SEP 2014
Accepted article online 22 SEP 2014
Published online 16 OCT 2014

Abstract The Earth's magnetosphere supports several types of ultralow frequency (ULF) waves. These include fast mode resonance (FMR): cavity modes, waveguide modes, and tunneling modes/virtual resonance. The magnetopause, often treated as the outer boundary for cavity/waveguide modes in the dayside magnetosphere, is not stationary. A rapidly changing outer boundary condition—e.g., due to rapid magnetopause motion—is not favorable for FMR generation and may explain the sparseness of FMR observations in the outer magnetosphere. We examine how magnetopause motion affects the dayside magnetosphere's ability to sustain FMR with idealized Space Weather Modeling Framework (SWMF) simulations using the BATS-R-US global magnetohydrodynamic (MHD) code coupled with the Ridley Ionosphere Model (RIM). We present observations of FMR in BATS-R-US, reproducing results from other global MHD codes. We further show that FMR is present for a wide range of solar wind conditions, even during periods with large and rapid magnetopause displacements. We compare our simulation results to FMR observations in the dayside magnetosphere, finding that FMR occurrence does not depend on solar wind dynamic pressure, which can be used as a proxy for dynamic pressure fluctuations and magnetopause perturbations. Our results demonstrate that other explanations besides a nonstationary magnetopause—such as the inability to detect FMR in the presence of other ULF wave modes with large amplitudes—are required to explain the rarity of FMR observations in the outer magnetosphere.

1. Introduction

At the lower end of the ultra low frequency range (ULF, frequency $\leq$ 5 Hz, [*Jacobs et al.*, 1964]) the Earth's magnetosphere supports several types of large-scale standing waves, or eigenmodes, that have scales comparable to the size of the magnetosphere. These waves can have coherent electric fields that interact with radiation belt electrons, potentially causing radial transport and affecting the population of relativistic electrons [e.g., *Elkington et al.*, 2003; *Hudson et al.*, 2014]. These eigenmodes include several types of fast mode resonance (FMR):

1. Cavity modes, where fast mode wave energy is trapped between an inner and outer boundary (e.g., plasmapause and magnetopause) and the magnetosphere is treated as a closed system [e.g., *Kivelson et al.*, 1984, 1997; *Hartinger et al.*, 2012].
2. Waveguide modes, where fast mode wave energy is trapped between an inner and outer boundary and the magnetosphere is treated as an open system where energy can leak down the magnetotail [e.g., *Samson et al.*, 1992; *Mann et al.*, 1998].
3. Tunneling modes/virtual resonance where fast mode waves are trapped in the magnetosphere but potentially cross boundaries such as the plasmapause [e.g., *Zhu and Kivelson*, 1989; *Lee and Lysak*, 1999; *Takahashi et al.*, 2010a].

All types of FMR share one important feature: they are affected by boundary motion. The frequencies and radial amplitude structure of the FMR depend on the boundary locations. *Kivelson et al.* [1997] proposed that rapid (on time scales comparable to a few FMR wave cycles), substantial (large enough to change FMR frequencies) boundary displacements could reduce the occurrence of FMR. This is one possible explanation for a rarity of FMR observations [*Engebretson et al.*, 1986], although alternative explanations—such as large damping rates or the inability to detect FMR in the presence of other ULF modes with large amplitudes and similar frequencies—are possible [*Kivelson et al.*, 1997].

Figure 1 shows representative cases for the effect of magnetopause boundary motion on FMR. The top shows a meridional view of the dayside magnetosphere where two field lines indicate a static inner

©2014. American Geophysical Union. All Rights Reserved.

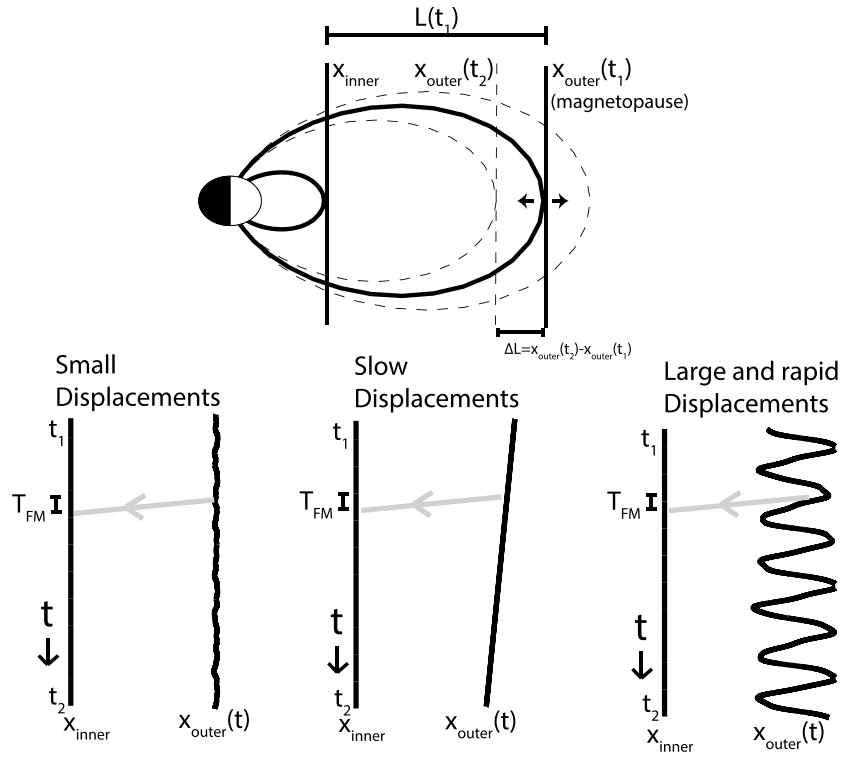

Figure 1. This figure shows a few representative cases for the effect of magnetopause boundary motion on FMR. (top) A meridional view of the dayside magnetosphere where two field lines indicate a static inner boundary for the FMR trapping region (x_{inner}, e.g., plasmapause) and the initial outer boundary of the FMR trapping region ($x_{outer}(t_1)$, the magnetopause). The outer boundary can move as a function of time, changing to a new position at time t_2 (indicated by the dashed lines) and causing the width of the cavity in x, $L(t_1)$, to change by an amount ΔL. (bottom) Three different types of boundary motion, with time going from top to bottom in each case—gray rays in each plot indicate the path of a propagating fast mode wave, and T_{FM} is the fast mode transit time between boundaries.

boundary for the FMR trapping region (x_{inner}, e.g., plasmapause) and the initial outer boundary of the FMR trapping region ($x_{outer}(t_1)$, the magnetopause)—x is for the distance from the Earth. The outer boundary can move as a function of time, changing to a new position at time t_2 (indicated by the dashed lines) and causing the width of the cavity in x, $L(t_1)$, to change by an amount ΔL. The bottom of the figure shows three representative types of boundary motion. The left is for small displacements compared to L (i.e., $\Delta L << L$). This is the usual case considered in numerical models where boundary motion provides energy for FMR, but ΔL is too small compared to L to affect FMR occurrence or properties; in other words, displacements of the outer boundary are assumed small compared to the dimensions of the wave trapping region and the boundary conditions do not change with time [e.g., *Kivelson et al.*, 1984; *Samson et al.*, 1992]. The middle is for substantial magnetopause displacements that are too slow compared to fast mode transit times across L, T_{FM}, to affect FMR occurrence. However, these displacements gradually change FMR properties. For example, the frequency changes as T_{FM} is reduced or increased since FMR periods are approximately proportional to the time of flight across the cavity. The bottom right of Figure 1 indicates a situation with large and rapid magnetopause displacements. In these cases, we expect the boundary motion to render the magnetosphere incapable of supporting FMR.

There is some evidence supporting the hypothesis that magnetopause motion substantially reduces FMR occurrence rates. *Allan et al.* [1991] used a box model simulation to show that FMR properties predicted by linear theory are substantially modified or nonexistent during periods with large and rapid magnetopause displacements, and *Hartinger et al.* [2013a] presented suggestive statistical evidence that during periods when large magnetopause displacements were expected, FMR occurrence rates decrease. However, it remains unclear whether typical magnetopause displacement amplitudes and speeds affect FMR occurrence and thus whether magnetopause motion can explain the rarity of FMR observations.

©2014. American Geophysical Union. All Rights Reserved.

Analytic models of FMR capture the essential features of these waves and have been successfully used to identify FMR in data [e.g., *Kivelson et al.*, 1984; *Samson et al.*, 1992; *Kivelson et al.*, 1997; *Waters et al.*, 2002; *Hartinger et al.*, 2013a]. However, boundary motion is difficult to self-consistently capture in analytic models of FMR; differential equations with boundary conditions that change as a function of time can only be solved for limited cases [e.g., *Balazs*, 1961]. Global MHD simulations, however, can realistically capture both magnetopause boundary motion and FMR [e.g., *Samsonov et al.*, 2007; *Claudepierre et al.*, 2009]. The purpose of this study is to determine how magnetopause boundary motion affects the occurrence and properties of FMR in the dayside magnetosphere using both global MHD simulations and satellite observations. Using simulations designed to explore nearly the full range of observed magnetopause displacement speeds and amplitudes, we shall demonstrate that magnetopause motion does not significantly affect FMR occurrence. We shall further support this claim using simultaneous satellite observations in the solar wind and magnetosphere showing that FMR occurrence rates do not change in different solar wind dynamic pressure regimes—and, by proxy, magnetopause motion regimes.

2. Methodology

2.1. Global MHD Simulations

To simulate FMR, we use the Space Weather Modeling Framework (SWMF), a scheme for coupling many different models used for different physics domains [*Tóth et al.*, 2005]. We run SWMF simulations using the Yellowstone supercomputer operated by the National Center for Atmospheric Research (NCAR) and the Kraken supercomputer operated by the National Institute for Computation Sciences and the Extreme Science and Engineering Discovery Environment (XSEDE). We only use two SWMF models for the present study: a single-fluid version of BATS-R-US [*Powell et al.*, 1999] for the magnetosphere coupled to the Ridley Ionosphere Model (RIM) [*Ridley and Liemohn*, 2002, 2004]. The coupling between BATS-R-US and RIM occurs by combining field-aligned currents mapped from the inner boundary of BATS-R-US, the $F_{10.7}$ flux (an input parameter held fixed in these simulations), and an empirical model to obtain conductances. Using a Poisson-type equation, electric potentials are then obtained on the RIM grid, and these are mapped back to the inner boundary of BATS-R-US.

In all simulations in this study, the ionosphere Pedersen conductivity in the RIM model is approximately 5 mho in the dayside ionosphere. This conductivity is high enough to support standing Alfvén waves, and it may be possible to couple FMR to these waves via the field line resonance (FLR) mechanism. In the simulation output, we found evidence of standing Alfén waves with two notable properties: (1) amplitude enhancements in the radial electric field that change frequency at different radial distances (not shown); these indicate a continuum of toroidal mode standing Alfvén wave frequencies driven directly by broadband frequency solar wind density fluctuations rather than by a monochromatic FMR and (2) much smaller amplitudes than the FMR. These properties indicate that the FLRs are not an important energy sink for FMR and do not affect FMR dynamics in the simulations. The topic of standing Alfvén waves/FLR in BATS-R-US will be explored in a separate study.

We focus exclusively on the analysis of BATS-R-US output for this study. BATS-R-US has been used to study a wide range of phenomena in the Earth's magnetosphere, including magnetopause motion and ULF wave activity with evidence of cavity modes [*Samsonov et al.*, 2007, 2011]. BATS-R-US coupled with RIM and an inner magnetosphere model has also been shown to faithfully reproduce ground magnetic perturbations associated with ionospheric currents [*Yu and Ridley*, 2011; *Pulkkinen et al.*, 2013]. BATS-R-US uses a Cartesian grid with variable grid cell size and an adjustable tilt for the Earth's dipole field. For the simulations in this study, we set the dipole parallel to the planetary rotation axis and use a simulation domain (SM coordinates) of x from −96 to 32 R_E, y from −64 to 64 R_E, and z from −64 to 64 R_E, where the inner boundary of BATS-R-US is a sphere of 2.5 R_E. In the region from $-16 \le x \le 32$, $-16 \le y \le 16$, and $-16 \le z \le 16$, the grid cells have widths of 1/8 R_E, with gradually increasing cell dimensions outside of this region.

All numerical models include numerical diffusion to varying degrees, and it is important to check whether this diffusion substantially affects the analysis of simulation data [e.g., *Ridley et al.*, 2010]. We examined the sensitivity of our results to grid cell dimensions by running a series of simulations with the same driving conditions (those specified in section 3.1.1) but different grids; the full results of this analysis are shown in the supporting information. The analysis shows that as long as grid cells are no larger than 1/4 R_E in the dayside magnetosphere, FMR is not substantially affected by numerical diffusion. Thus, 1/8 R_E resolution is sufficient to capture FMR activity in the dayside magnetosphere (see supporting information for more description

©2014. American Geophysical Union. All Rights Reserved.

of the grid resolution). We also checked the sensitivity of our results to the "Boris Correction" factor, which is commonly used in global MHD simulations (e.g., BATS-R-US, [*Gombosi et al.*, 2002]; LFM, [*Claudepierre et al.*, 2009]) to artificially reduce the speed of light [*Boris*, 1970]. This correction slows the maximum wave speed in the simulation and inhibits numerical diffusion [*Powell et al.*, 1999; *Lyon et al.*, 2004]. We found that a correction of 0.05 (i.e., speed of light reduced by a factor of 20) worked well, but we also tried values of 0.02 and 0.1; varying the correction factor by these amounts did not significantly affect our results (see supporting information).

In all simulations, we output wave quantities (e.g., electric field) at different spatial positions every 10 s. We use Fourier analysis to examine the spatial structure and time evolution of wave activity using both power spectral densities (PSD) and the square root of the PSD normalized to its maximum value; the latter is equivalent to the normalized root-mean-square (RMS) wave amplitude. To obtain PSD, we first extract a time series for a parameter of interest at a given spatial position. Next, we divide the time series into overlapping 1024 point segments (171 min—there is a shift of 64 points, or 11 min, between each segment), and we obtain the PSD for each 1024 point segment.

We reduce error in the PSD estimate by averaging over both frequency and time. In particular, we divide each 1024 point segment into four overlapping 512 point (85 min) segments: 0 to 512, 171 to 683, 342 to 854, and 512 to 1024. We compute the PSD for each smaller 512 point segment, smoothing over adjacent frequency bins with a six-point window as the first step in reducing error: we thus obtain four separate estimates of the PSD (one for each 512 point segment) for the larger 1024 point segment. Finally, we further reduce error in the PSD estimate for each 1024 point segment by taking the mean value (at each frequency) of the PSD over the four 512 point windows.

2.2. GOES and Wind Satellite Observations

We use a database constructed by *Viall et al.* [2009] to examine the occurrence of discrete frequency pulsations in the solar wind density and dayside magnetosphere magnetic field. *Viall et al.* [2009] used 11 years (1995–2005) of 100 s resolution density data from the Solar Wind Experiment on the Wind spacecraft [*Ogilvie et al.*, 1995] and 10 years (1996–2005) of 60 s resolution data from the vertical component (usually approximates SM *z*) of the magnetic field from the fluxgate magnetometer on the GOES-8, GOES-9, and GOES-10 satellites [*Singer et al.*, 1996]. Both the GOES and Wind data were organized into 6 h segments with adjoining segments shifted by 10 min. All Wind data that included shocks, discontinuities, data jumps, data gaps, and data obtained inside the magnetosphere were excluded; only periods when Wind was within 200 R_E of the Earth-Sun line were included (ballistically propagated measurements must be within 35 R_E of the Earth-Sun line upon reaching the magnetosphere). These analysis periods were further reduced by requiring that only GOES 6 h segments with a mean time within 3 h of local noon were analyzed, restricting the analysis to the dayside magnetosphere. If more than one GOES probe was located within 3 h of noon, only measurements from the probe closest to noon were used; if no GOES probes met this criterion, the period was not analyzed. Each segment was Fourier analyzed to identify significant spectral peaks corresponding to discrete frequency wave activity in the magnetosphere and solar wind—see *Viall et al.* [2008] and *Viall et al.* [2009] for a full description of the identification of these peaks.

The combination of solar wind (Wind) and magnetosphere (GOES) observations allows us to categorize wave activity and identify potential FMR events. For the purposes of this study, all 6 h segments examined by *Viall et al.* [2009] where both GOES and Wind data available were divided into five categories according to wave properties in the 4–5 mHz frequency range:

1. Both Wind and GOES have a discrete frequency peak at the same frequency. These represent events that are directly driven by the solar wind (i.e., not FMR, [*Kepko et al.*, 2002]). There are 4497 data segments in this category at 4–5 mHz.
2. Both Wind and GOES have a discrete frequency peak, but not at the same frequency. These may be FMR. There are 2547 segments in this category at 4–5 mHz.
3. GOES has a discrete frequency peak but not Wind. These are likely FMR. There are 22,286 segments in this category at 4–5 mHz.
4. Wind has a discrete frequency peak but not GOES. These are not FMR. There are 7588 events in this category at 4–5 mHz.
5. Neither Wind nor GOES have discrete frequency peaks. These are not FMR. There are 23,856 events in this category at 4–5 mHz.

©2014. American Geophysical Union. All Rights Reserved.

Table 1. Categories for GOES and Wind Satellite Events Based on Whether One or Both Satellites Observed Discrete Frequency Waves at 4–5 mHz, Whether They Have the Same or Nearly the Same Frequency Peak, and Whether the Category Includes FMR Events

Category	Wind Peak	GOES Peak	Frequency	FMR	Number of Segments
1	Yes	Yes	Same	No	4,497
2	Yes	Yes	Close	Maybe	2,547
3	No	Yes	N/A	Likely	22,286
4	Yes	No	N/A	No	7,588
5	No	No	N/A	No	23,856

These categories are summarized in Table 1. The 4–5 mHz frequency range was chosen for two reasons. The first is that the fundamental FMR frequencies we find in the last two simulations are close to this frequency. The second is that this range is below the Nyquist frequency based on the Wind sampling rate; 4–5 mHz is the highest frequency range where it is possible to conduct this analysis.

The *Viall et al.* [2009] events were identified at geostationary orbit based solely on the power spectrum of the vertical component of the magnetic field perturbation, which ought to be associated with FMR, since FMR waves are compressional. However, it is possible that some non-FMR events were identified, such as compressional Alfvén waves or propagating fast mode waves from the ion foreshock. We do not expect these waves to be a significant source of error for two reasons. First, standing Alfvén wave frequencies are typically larger than 5 mHz at geostationary orbit. Assuming a proton plasma with density of 1 amu per cc at geostationary orbit and a realistic field geometry, the fundamental standing Alfvén wave period in the dayside magnetosphere is roughly 20 mHz [*Singer et al.*, 1981]; if the density is increased by an order of magnitude, this would decrease the frequency to roughly 6 mHz based on the Alfvén wave time of flight. Thus, apart from solar maximum conditions—when geostationary mass densities can be much larger leading to frequencies comparable to or below 5 mHz [*Takahashi et al.*, 2010b]—4–5 mHz ought to be below the standing Alfvén wave frequency.

The second reason we do not expect non-FMR events to be a major source of error is that propagating upstream waves from the ion foreshock—which may mimic the expected signature of FMR in the *Viall et al.* [2009] database but do not necessarily have to couple to FMR—typically occur at frequencies above the 4–5 mHz range [*Troitskaya et al.*, 1971]. It is possible that other transient phenomena in the ion foreshock could generate compressional wave activity at geostationary orbit that is unrelated to FMR. However, these waves would not be identified using the *Viall et al.* [2009] methodology unless they excited a monochromatic FMR, since they are impulsive and lead to an initial ULF response with a broadband frequency spectrum [*Hartinger et al.*, 2013b].

We examine the occurrence rate of events in these five categories as a function of average solar wind dynamic pressure, which can be used as a proxy for dynamic pressure fluctuations in the Pc5 frequency range (2–7 mHz) and, potentially, magnetopause displacement amplitude [*Takahashi and Ukhorskiy*, 2007; *Hartinger et al.*, 2013a]. We use 6 h averages (the Wind/GOES event window) for the background dynamic pressure, whereas *Takahashi and Ukhorskiy* [2007] and *Hartinger et al.* [2013a] used hourly averages. To avoid biases caused by uneven sampling during different solar wind pressure regimes, we bin according to dynamic pressure before calculating occurrence rates. In each bin, we divide the number of events in a given category by the total number of events in the bin to obtain the occurrence rate.

3. Results

In the first part of this section, we examine the effect of magnetopause motion on FMR using idealized global MHD simulations. In the second part of this section, we examine Wind and GOES satellite data to further examine how magnetopause motion affects FMR.

3.1. The Effect of Magnetopause Motion on Fast Mode Resonance: Simulation Results

In the next three subsections, we show results from three idealized global MHD simulations of FMR in the dayside magnetosphere, corresponding to the three cases in Figure 1.

3.1.1. Small Magnetopause Displacements

Our first goal in this study is to demonstrate that the BATS-R-US model can capture FMR by reproducing results obtained using the Lyon-Fedder-Mobarry (LFM) model, a different global MHD simulation code.

©2014. American Geophysical Union. All Rights Reserved.

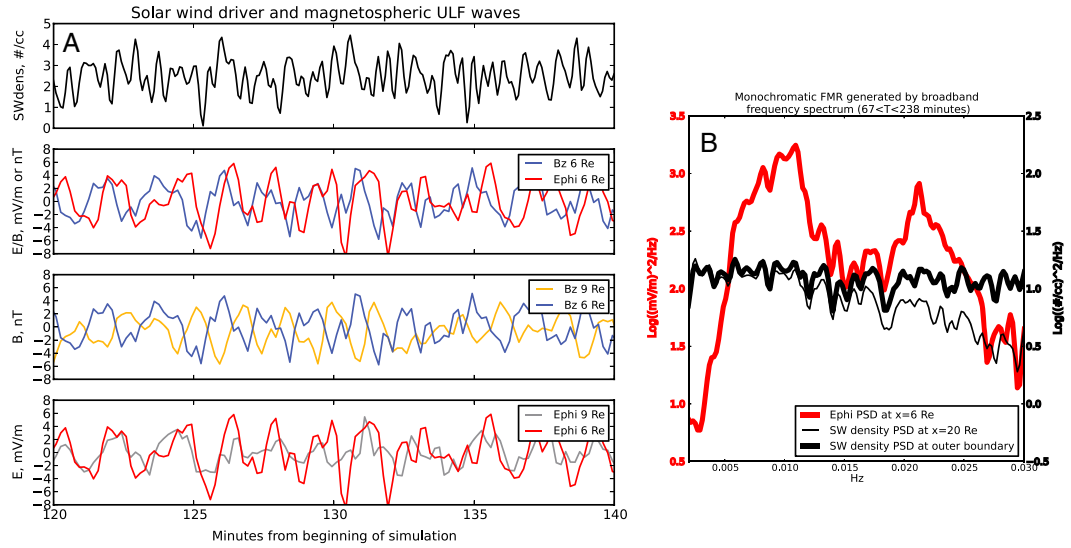

Figure 2. This figure shows output from a simulation with driving conditions nearly identical to *Claudepierre et al.* [2009] (see top row of Table 2 for simulation driving conditions). (a) From top to bottom, the solar wind density, the east-west electric field (E_ϕ, red line), and SM z (compressional) magnetic field perturbations (b_z, blue line) at r = (6,0,0) R_E, b_z at r = [6,0,0] (red line) and r = [9,0,0] (black line) R_E, and E_ϕ at r = [6,0,0] (red line) and r = [9,0,0] (black line) R_E. (b) A comparison between the r = [6,0,0] R_E E_ϕ power spectrum (red line) and the solar wind density power spectrum at the outer boundary (bold black line) and r = [20,0,0] R_E (faint black line).

Figure 2 shows output from a simulation with driving conditions nearly identical to the LFM continuum run of *Claudepierre et al.* [2009]: solar wind $\mathbf{B} = (0, 0, -5)$ nT, solar wind $\mathbf{V} = (-600, 0, 0)$ km/s, solar wind density $n(t) = n_0 + 0.05 \sum_{j=0}^{500} sin(\omega_j t + \phi_j)$ (t is for time, n_0 is the background density of 2.5 amu per cc, ω is frequency, ϕ is phase which is varied randomly in the sum, and the sum is over the 0 to 50 mHz band in steps of 0.1 mHz between frequency components, so j is from 0 to 500), the background sound speed in the solar wind is 40 km/s, and an out-of-phase oscillation is added to the background sound speed (via temperature perturbations) to maintain constant solar wind thermal pressure. The only difference between the driving conditions of *Claudepierre et al.* [2009] and this simulation is in n_0; we chose a smaller value (2.5 compared to 5 amu per cc) to obtain a similar equilibrium magnetopause location as in *Claudepierre et al.* [2009] (at 5 amu per cc, the subsolar BATS-R-US magnetopause was at a smaller radial distance when compared to the *Claudepierre et al.* [2009] results). The driving conditions in this simulation, and the other simulations used in this study, are summarized in the top row of Table 2. We used the simulation grid with the highest resolution/largest number of grid cells for this simulation (and all other simulation results in this study); grid cells have dimensions of 1/8 R_E throughout the dayside magnetosphere (see supporting information for further detail).

This simulation is most similar to the situation in the leftmost portion of Figure 1: small displacements of the magnetopause. Figure 2a shows, from top to bottom: the solar wind density; the ϕ component (east-west) of the perturbation electric field in SM cylindrical coordinates (E_ϕ, red line), and the SM z perturbation magnetic field (b_z, blue line) at r = (6,0,0) R_E; b_z at r = [6,0,0] (blue line) and r = [9,0,0] (light orange line) R_E; and E_ϕ at r = [6,0,0] (red line) and r = [9,0,0] (gray line) R_E. The perturbations exhibit several key features of cavity modes, a type of FMR: 90° phase difference between E_ϕ and b_z, 180° phase shifts between b_z but not E_ϕ, indicating the presence of a magnetic field node between the two observation points, and monochromatic perturbations in the presence of a driver with a broadband frequency spectrum. Figure 2b shows a comparison between the r = [6,0,0] R_E E_ϕ PSD (red line) and the solar wind density PSD at the outer boundary (bold black line) and r = [20,0,0] R_E (faint black line—as discussed in the supporting information, there is some attenuation of the highest-frequency solar wind density perturbations between the outer boundary at r = [32,0,0] and r = [20,0,0] due to grid resolution). As in Figure 2a, there is clear evidence of FMR: monochromatic waves in the magnetosphere are generated by waves with a broadband frequency spectrum in the solar wind.

©2014. American Geophysical Union. All Rights Reserved.

Table 2. Summary of the Simulation Driving Conditions in This Study[a]

Simulation	$n(t)$ (cm^{-3})	B_z (nT) [b]	V_x (km/s) [c]
1	$2.5 + 0.05 \sum_{j=0}^{500} \sin(\omega_j t + \phi_j)$ [d]	−5	−600
2	$n_0(t) + A_1(t)\Sigma_j \sin(\omega_j t + \phi_j)$ [e]	5	−500
3	$10 + 0.05\Sigma_j \sin(\omega_j t + \phi_j) + A_2(t) \sin(\omega_0 t)$ [f]	5	−400
3a	$10 + A_2(t) \sin(\omega_0 t)$ [f]	5	−400

[a]In all simulations, the background sound speed in the solar wind is 40 km/s, and an out-of-phase oscillation is added to the background sound speed (via temperature perturbations) to maintain constant solar wind thermal pressure.
[b]$B_x = B_y = 0$ in all simulations.
[c]$V_y = V_z = 0$ in all simulations.
[d]$\omega_j = 2\pi \times 0.0001 \times j$ rad/s, ϕ_j is a random phase shift.
[e]$n_0(t) = 1$, $t < 4$ h; $n_0(t) = 1 + 14\frac{t-4}{16}$, $t \geq 4$ h; $A_1(t) = 0.0012 \times n_0(t)^{1.89}$.
[f]$A_2(t) = 0$, $t < 3$ h; $A_2(t) = 8\frac{t-3}{6.5}$, $t \geq 3$ h.

We found very similar results to *Claudepierre et al.* [2009] that are expected for cavity mode FMR: (1) monochromatic E_ϕ perturbations in the magnetosphere in the presence of a driver with a broadband frequency spectrum, (2) nodal structure, and (3) multiple wave harmonics. One notable difference is the radial amplitude structure of the FMR: *Claudepierre et al.* [2009] found evidence for a quarter-wavelength fundamental, whereas in this study we find that the fundamental is a half-wavelength standing wave with a magnetic field node outside geostationary orbit. This is indicated by the 180 phase shift shown in the third panel of Figure 2a and in later figures that show the radial amplitude profile of E_ϕ peaking inside the magnetosphere. This disparity is reasonable, since there are a few important differences between the *Claudepierre et al.* [2009] LFM simulations and this BATS-R-US simulation that we cannot control, such as the sharpness of the Alfvén speed gradient at the magnetopause, which affects the reflection of fast mode waves.

To summarize, BATS-R-US supports FMR during conditions with small magnetopause displacements driven by solar wind density perturbations, as expected from previous modeling results. We note that the typical amplitudes for FMR found in the BATS-R-US simulations are similar to *Claudepierre et al.* [2009] (on the order of 1 nT and 1 mV/m—compare the rightmost panel of Figure 2 in *Claudepierre et al.* [2009] to Figure 2 in this study), showing that there are no sources of numerical diffusion unique to BATS-R-US that preclude a realistic description of FMR.

3.1.2. Slow Magnetopause Displacements

In this section, we show results from a simulation designed to quantify the effect of magnetopause motion on FMR in the dayside magnetosphere for the situation indicated in the bottom middle of Figure 1. This simulation serves two purposes: (1) examine how slow but substantial displacements of the magnetopause boundary affect FMR, (2) use a realistic scaling between the background and perturbation density in the solar wind to examine how magnetopause motion affects FMR in different solar wind driving regimes (i.e., explore parameter space). We use the same version of BATS-R-US as in the previous section, but with different driving conditions summarized in the second row of Table 2.

In this simulation, the amplitude of the density perturbations, $A(t)$, changes as a function of time. $A(t)$ was chosen to be consistent with correlations that are observed between background solar wind dynamic pressure and Pc5 solar wind dynamic pressure fluctuations [*Takahashi and Ukhorskiy*, 2007; *Hartinger et al.*, 2013a]. For the first 4 h of the simulation, $n_0(t)$ is held fixed at 1 per cc; then it increases gradually to 15 per cc for the last 16 h of the simulation. We also chose a northward IMF driving condition, rather than southward as in the previous simulation, to reduce the chances of transient dayside reconnection occurring in the simulation. The velocity was reduced to 500 km/s (from 600 km/s in the previous simulation) to represent a more typical value for the solar wind speed.

The top part of Figure 3 shows the time evolution of the solar wind density driver and the resulting ULF wave activity in the magnetosphere. The first panel is for the solar wind density at r=(20,0,0) R_E, and the second panel is for the corresponding dynamic power spectrum. These two panels show that the wave energy delivered to the magnetosphere increases as a function of time and has a broadband frequency spectrum apart from some attenuation at higher frequencies caused by numerical dissipation

©2014. American Geophysical Union. All Rights Reserved.

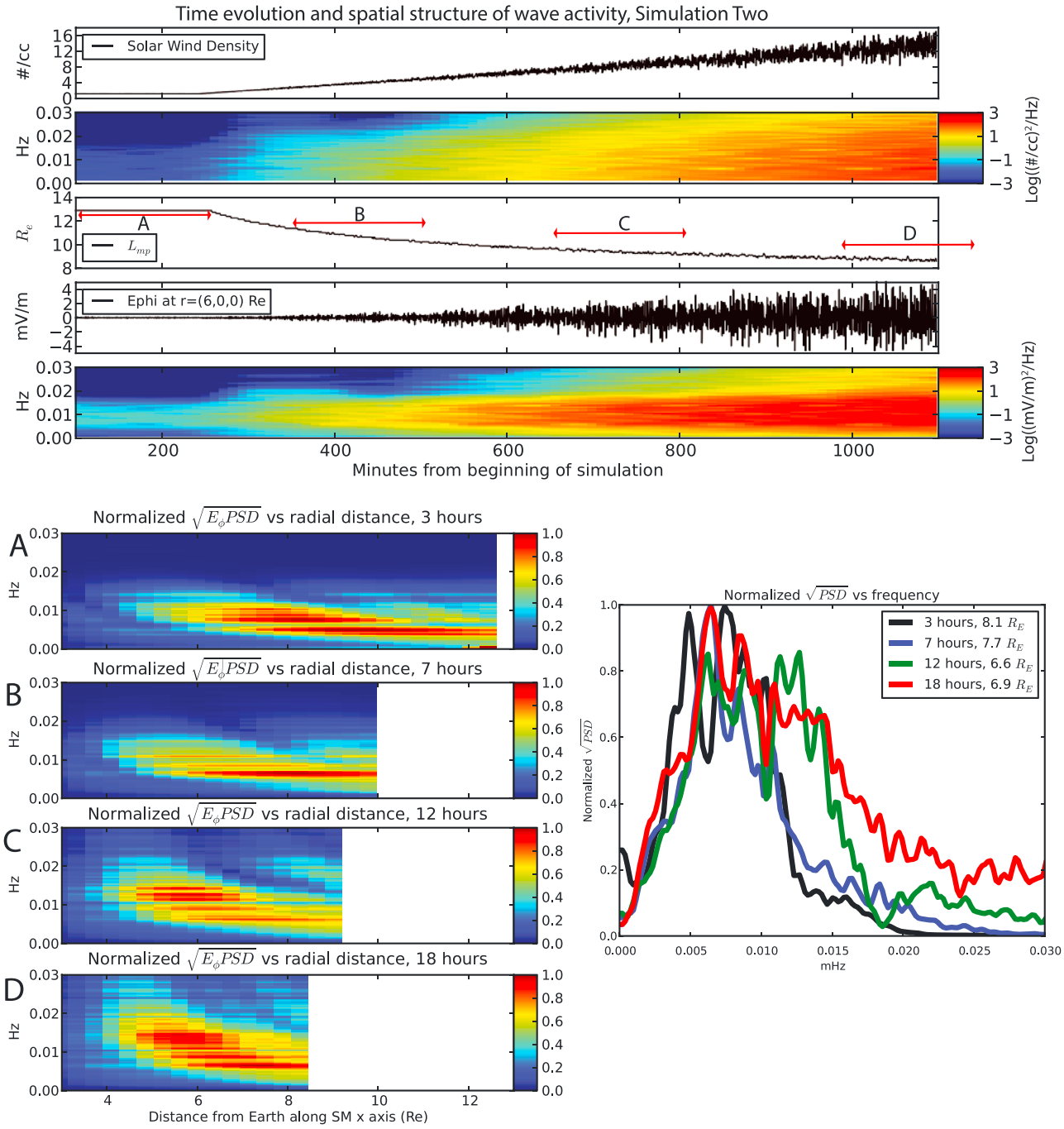

Figure 3. (top) From top to bottom, solar wind density at r = (20,0,0) R_E, dynamic power spectrum for the solar wind density, the magnetopause location on the SM x axis, the electric field ϕ perturbation, and the dynamic power spectrum for the electric field (all for simulation 2—see the second row of Table 2 for simulation driving conditions). (bottom left) Normalized $\sqrt{E_\phi}$PSD is shown as a function of radial distance along the SM x axis and frequency—the data in each panel are normalized to the maximum value in the 5 to 30 mHz frequency range and radial distances between r = (3,0,0) and r = (L_{MP},0,0). From top to bottom, data from a ~170 min interval centered at 3 h (interval (a) in Figure 3 (top)), (b) 7 h, (c) 12 h, and (d) 18 h. (bottom right) Slices from the figure at left of normalized $\sqrt{E_\phi}$PSD at radial distances corresponding to the peak electric field amplitude at 7.8 mHz.

©2014. American Geophysical Union. All Rights Reserved.

(see supporting information). The next panel is for the magnetopause location along the SM *x* axis. The magnetopause was identified as the location with the largest radial pressure gradient and current density. As expected, the magnetopause slowly moves inward as the solar wind density increases. There are also small, but noticeable, perturbations in the magnetopause location caused by the solar wind density fluctuations. These perturbations ought to drive magnetospheric ULF wave activity, and the next panel - showing the E_ϕ perturbation at r=(6,0,0) R_E - demonstrates this. The amplitude of the E_ϕ perturbation increases along with the increasing solar wind density fluctuations. Finally, the bottom panel shows the dynamic power spectrum for E_ϕ. There is an enhancement in wave activity at ~5-15 mHz; this enhancement is not present in the solar wind density (second panel) and indicates the presence of FMR, as in Figure 2b.

More information on the spatial structure of wave activity is shown on Figure 3 (bottom left). Here each panel shows the normalized square root of the power spectral density for E_ϕ ($\sqrt{E_\phi \mathrm{PSD}}$) as a function of frequency and radial distance along the SM *x* axis. $\sqrt{E_\phi \mathrm{PSD}}$ is normalized to the maximum value in the 5 to 30 mHz frequency range and radial distances between r = (3,0,0) and r = (L_{MP},0,0); this normalization allows us to focus on changes to the FMR amplitude structure rather than the slow, frequency-independent increase in the PSD (this increase is seen most clearly in the top part of Figure 3, bottom left). Different panels are for different 170 min time intervals (fast Fourier transform (FFT) windows) indicated by the red lines in panel three of the top figure. Note that the top figure only shows a 16.7 h interval (100–1100 min) for the full 20 h simulation (that is why the arrows extend past the end of the panel); this subset was chosen so the center of the first and last FFT window would not be inside the time range shown, reducing whitespace.

In Figure 3a, corresponding to the 170 min time interval centered on the third hour of the simulation, there are clear peaks in $\sqrt{E_\phi \mathrm{PSD}}$. The clearest peak is narrow (in frequency) at ~5 mHz and seen most strongly as a red band between 7 R_E and the magnetopause. The peak has the same frequency at a wide range of radial distances, as expected for FMR but not for many other ULF wave modes such as standing Alfvén waves [e.g., *Waters et al.*, 2002]. We conducted similar tests (not shown) as in section 3.1.1 to confirm this as FMR. As expected, the perturbation magnetic field *z* component was 90° out of phase with the electric field and had the expected amplitude structure at the FMR frequency (nodes at the electric field antinodes).

At later times in the simulation, the amplitude structure changes. For example, the next panel (Figure 3b) is for the time interval centered at 7 h; the low-frequency peak is still present, while the higher frequency peak is not as strong. Note that we have masked radial distances corresponding to locations outside the magnetopause, which has moved in to roughly 10 R_E by this time in the simulation. As the solar wind background density and density fluctuations increase in the next two panels, the low frequency peak is always seen but changes its frequency slightly, while higher frequency peaks are present but change their radial structure and bandwidth more substantially as the solar wind driver changes. We reiterate here that all of these peaks in $\sqrt{E_\phi \mathrm{PSD}}$ are not included in the driving conditions in the solar wind (see Figure 3 (top), second panel): they are FMR eigenmodes of the magnetosphere. The spectral feature corresponding to the fundamental FMR is present at all times in this simulation; this indicates that the magnetopause displacements do not affect FMR occurrence. We return to this point in section 4.

A shift in the fundamental FMR frequency is seen in Figure 3 (bottom right). Here the normalized $\sqrt{E_\phi \mathrm{PSD}}$ is shown at the same four time intervals as in Figure 3 (bottom left), but only for the radial distances corresponding to the $\sqrt{E_\phi \mathrm{PSD}}$ peak at the FMR frequency. The black curve, corresponding to the third simulation hour, has the lowest frequency peak at 5 mHz, whereas the next three time periods have the first peak at roughly 7.5 mHz. The frequency change is caused by a number of factors that include the reduction in size of the cavity caused by the inward displacement of the magnetopause as well as changes to the radial Alfvén speed profile. As the magnetopause moves inward and is perturbed in response to the solar wind density variations, the magnetic field and plasma mass density in the magnetosphere also change. This is shown in Figure 4a, where each curve is for the Alfvén speed as a function of distance along the SM *x* axis and the different colored curves represent the Alfvén speed for the different intervals shown in Figure 3. The radial Alfvén speed profile changes substantially during the course of the simulation as the magnetic field and density change. This explains some of the frequency variations (or lack thereof) of the FMR as the magnetopause moves inward. One would generally expect the FMR frequency to increase as the magnetopause moves inward and the cavity size, and thus T_{FM}, decreases. However, this effect is countered by a systematic decrease in the Alfvén speed observed during the course of the simulation which increases T_{FM}. These two

©2014. American Geophysical Union. All Rights Reserved.

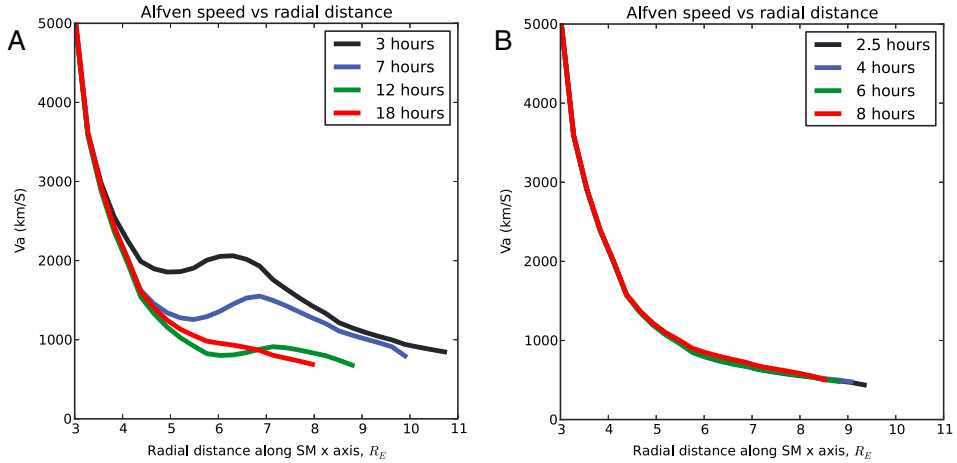

Figure 4. (a) The Alfvén speed is shown as a function of radial distance along the SM *x* axis at four different times during simulation two. Data at each time are averaged over a 170 min interval centered at that time, corresponding to the intervals a, b, c, and d in Figure 3. (b) The same as Figure 4a but for simulation three.

competing effects—the shrinking cavity size and the decreasing wave speed—are what ultimately lead to the change, or lack thereof, in the frequency of the fundamental FMR in these simulations.

Why does the Alfvén speed decrease during this simulation? In BATS-R-US simulations with northward IMF, plasma temperatures tend to be lower [e.g., *Welling and Ridley*, 2010]; as a result, we observed that most plasma in the dayside magnetosphere was corotating. As the magnetopause was compressed on timescales of an hour or two, there was no substantial loss of the corotating plasma in the dayside magnetosphere through the magnetopause, and thus the density increased as the volume decreased. Thus, a reduced magnetospheric volume increased the plasma mass density enough to substantially decrease the Alfvén speed during this simulation. We reiterate here that while both the changing magnetopause location and Alfvén speed affected the FMR properties in this simulation, neither precluded the occurrence of FMR.

3.1.3. Large and Rapid Magnetopause Displacements

In this section, we show results from a simulation designed to examine how rapid and substantial displacements of the magnetopause boundary affect FMR. We use the same version of BATS-R-US as in the previous two simulations but with different driving conditions summarized in the third row of Table 2. The amplitude of a 10 min period wave, $A(t)$, is 0 for the first 3 h of the simulation, then gradually increases to 8 per cc for the last 6.5 h of the simulation. This scaling was chosen so there would be substantial magnetopause displacements comparable to FMR timescales at the end of the simulation. The background density, n_0, is held fixed at 10 per cc. The magnetopause displacement amplitudes and speeds (maximum 8.9–12.2 R_E and 162 km/s, respectively) that result from these driving conditions are representative of nearly the full range of amplitudes and speeds observed at the dayside magnetopause [*Plaschke et al.*, 2009].

Analysis of wave activity during the latter part of this simulation presented unique challenges not present in the first two simulations: signal processing artifacts due to the presence of nonsinusoidal wave activity. To address this, we ran a simulation identical to the one described in the preceding paragraph except for the absence of density fluctuations with a broadband frequency spectrum, as summarized in the bottom row of Table 2. Nonsinusoidal wave activity is due primarily to the large amplitude, 10 min period solar wind density driver, and corresponding magnetopause displacements. These are present in both simulations, but only one simulation has the additional broadband frequency density fluctuations necessary to drive FMR. As we shall discuss, this difference allows us to remove signal processing artifacts from the first simulation and isolate the effect of the magnetopause displacements on FMR.

Figure 5 (top) presents an overview of wave activity in the same format as Figure 3. It shows the time evolution of the solar wind density driver and the resulting ULF wave activity in the magnetosphere. Black lines are for the simulation that includes broadband frequency density fluctuations, whereas red lines are for the simulation without these fluctuations. The top panel shows that wave energy delivered to the magnetosphere increases as a function of time at 1.67 mHz (the imposed 10 min period wave). This is also reflected in the second panel (for the simulation that includes the broadband frequency density fluctuations), where the

©2014. American Geophysical Union. All Rights Reserved.

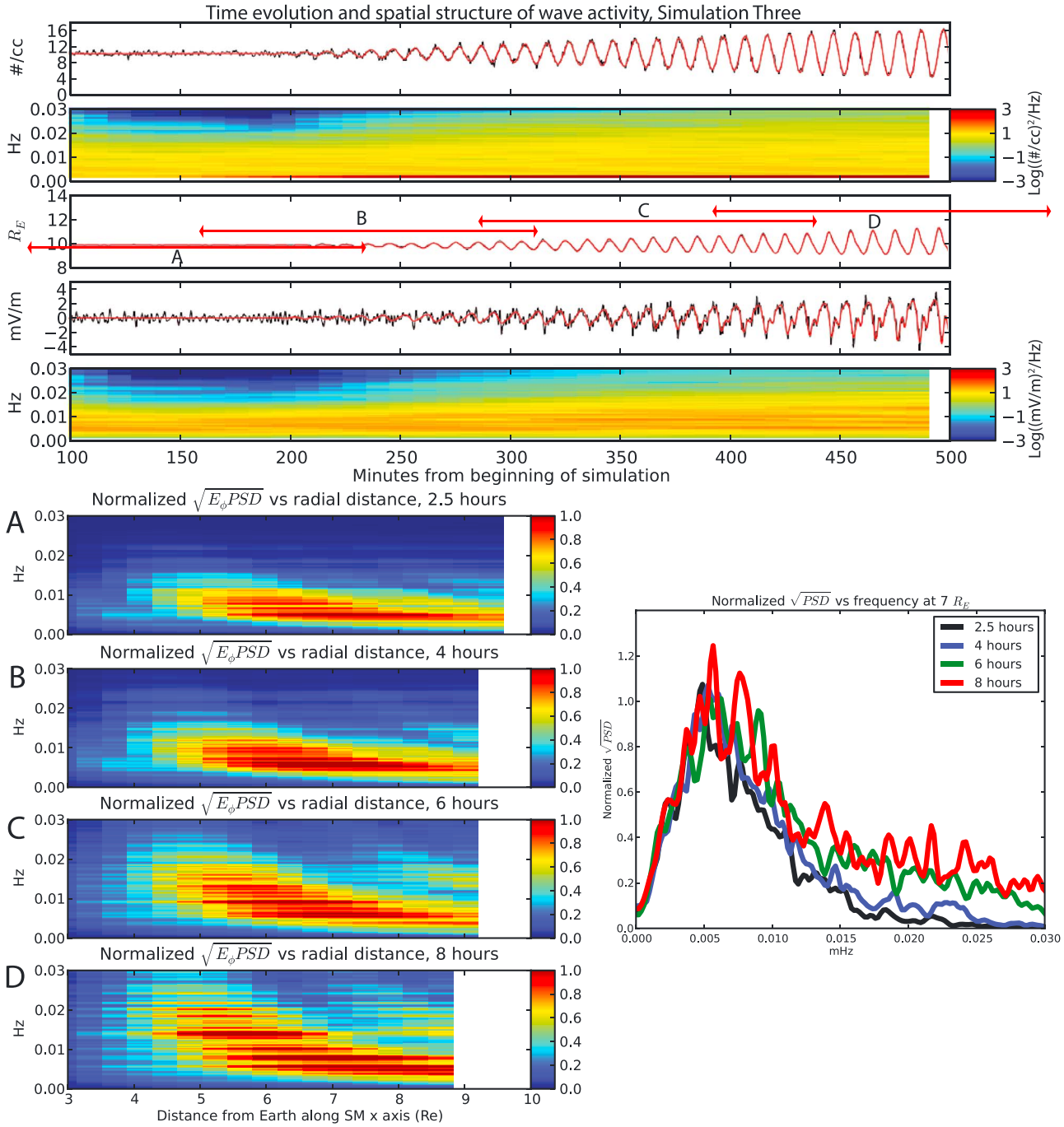

Figure 5. The same format as Figure 3 but for simulation three (see the bottom two rows of Table 2 for the driving conditions used in this simulation). Unlike Figure 3, the $\sqrt{E_\phi}$PSD in the bottom part of the figure are all normalized to the same value, the maximum value found during the first data interval. In the bottom right, the slices of normalized $\sqrt{E_\phi}$PSD are all from r = (7,0,0) R_E.

PSD at 1.67 mHz gradually increases and saturates the color scale. The third panel is for the magnetopause location along the SM x axis; as the amplitude of the sinusoidal solar wind density variation increases, so too does the amplitude of the magnetopause displacements. In contrast to the previous simulation, the equilibrium position of the magnetopause remains the same, but the magnetopause moves in and out with the solar wind density. The equilibrium position of the magnetopause on the x axis is at roughly 10 R_E, with a minima at 8.9 R_E and maxima at 12.2 R_E (note that the simulation continues for 570 min, and the maximum occurs past the end of the plot window in Figure 5). The maximum speed of the magnetopause during these

©2014. American Geophysical Union. All Rights Reserved.

oscillations is 162 km/s. Also note that the red and black lines are identical, indicating that the 10 min period wave in the solar wind density— present in both simulations—drives these magnetopause displacements.

The black and red lines in the fourth panel of Figure 5 (top) show the E_ϕ perturbation at r = (6,0,0) R_E. Nonsinusoidal variations with the periodicity of the 10 min solar wind driver become stronger near the end of the simulation due to nonlinear effects that arise when the amplitude of magnetic field perturbations are a significant fraction of the background magnetic field strength. Fourier series used to represent such signals (i.e., with rapid, nonsinusoidal variations) do not converge uniformly (Gibbs phenomena, e.g., *Kusse and Westwig* [1998], Chapter 7), leading to harmonics in power spectra that may overlap the FMR frequency band yet may not be related to the FMR. We found that this was the case when examining the power spectra of the E_ϕ time series; the E_ϕ PSD had large, nonphysical peaks at harmonics of the 10 min driver that were neither present in the solar wind nor representative of a superposition of sinusoidal wave activity in the magnetosphere.

The black (simulation with broadband density fluctuations) and red (simulation without broadband density fluctuations) lines in the fourth panel of Figure 5 both have nonsinusoidal fluctuations due to the large amplitude driver. It is not clear if these 10 min periodicity variations affect the smaller period FMR. To make this determination, we subtract the red line from the black line, removing the parts of the E_ϕ signal that lead to signal processing artifacts while retaining the part of the signal corresponding to FMR wave activity; in other words, we use the simulation without broadband density fluctuations to detrend the E_ϕ signal and isolate the FMR wave activity, removing lower frequency variations that contaminate the analysis of higher frequencies via the Gibbs phenomena. The bottom panel of Figure 5 (top) is for the PSD of the detrended E_ϕ signal. As in Figure 3, there is an enhancement in PSD corresponding to an FMR at roughly 5–15 mHz.

The spatial structure of wave activity of the detrended E_ϕ perturbation is shown on Figure 5 (bottom left) as in Figure 3 (bottom left) but with a difference pertaining to the normalization convention. As before, we normalize $\sqrt{E_\phi \mathrm{PSD}}$ to the maximum value in the 5 to 30 mHz frequency range and radial distances between r = (3,0,0) and r = (L_{MP},0,0), but we use the same normalization factor for all four panels: the maximum value during the first time interval. The top panel corresponds to the 170 min time interval centered on 2.5 h simulation time (interval a in Figure 5 (top)). Note that the top figure only shows a 6.7 h interval (100–500 min) for the 10 h simulation (that is why the arrows extend past the beginning and end of the panel); this subset was chosen so the center of the first and last FFT window would not be too far inside the time range shown, reducing whitespace. As in the previous simulation, there is a clear peak at ~5 mHz seen most strongly as a red band between 6 R_E and the magnetopause. In the next panel, for the time interval centered on the fourth simulation hour, the fundamental FMR is still present and its frequency and spatial extent are relatively unchanged. Figure 4b shows that the Alfvén speed profile effectively does not change during this simulation, unlike the previous simulation. Thus, the main factor that determines changes in the wave activity during the course of the simulation is the magnetopause motion.

The third and fourth panels on Figure 5 (bottom left) show qualitatively similar behaviors to the first two panels: PSD enhancements at discrete frequencies in the 5–15 mHz frequency range. However, there are some differences; PSD enhancements in the FMR frequency range become wider in frequency, and the PSD peak corresponding to the fundamental FMR becomes less well defined later in the simulation. This is also shown clearly in Figure 5 (bottom right), which has the same format as Figure 3 (bottom right). Higher-frequency waves have larger amplitudes relative to lower frequency waves near the end of the simulation, making the fundamental FMR peak broader. Despite these effects, the essential features of FMR predicted by linear theory—discrete frequency enhancements in the presence of a driver with a broadband frequency spectrum, radial amplitude structure with local minima and maxima [e.g., *Waters et al.*, 2002]—are still present in the latter portions of the simulation, when magnetopause displacement amplitudes and speeds are near the upper end of what has been observed at the dayside magnetopause [*Plaschke et al.*, 2009]. Surprisingly, the FMR is not strongly affected by the large, rapid magnetopause displacements present in this simulation.

3.2. The Effect of Magnetopause Motion on Fast Mode Resonance: Observations

Viall et al. [2009] conducted a statistical study of monochromatic ULF wave events in the solar wind and at geostationary orbit. As noted in section 2.2, they identified 22,286 monochromatic ULF wave events at geostationary orbit with frequencies of 4–5 mHz that did not have a counterpart in the solar wind. Figure 6 shows the occurrence rate for these waves versus averages of solar wind dynamic pressure (black line). As in *Hartinger et al.* [2013a], we assume that the averaged dynamic pressure can be used as a proxy for

©2014. American Geophysical Union. All Rights Reserved.

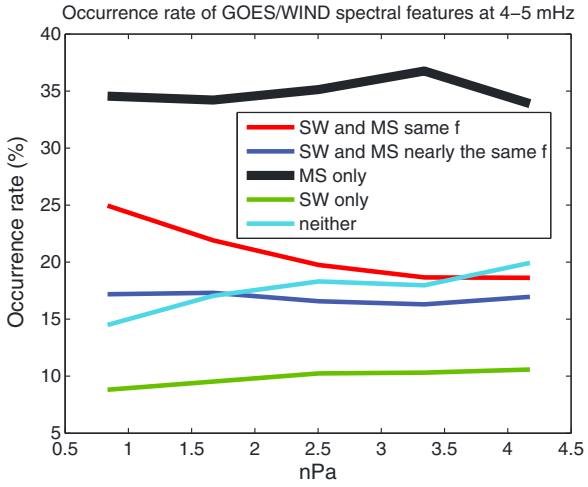

Figure 6. This figure compares the occurrence rates for different types of 4–5 mHz wave activity versus solar wind dynamic pressure: (1) a peak in power spectral density (PSD) is observed at the same frequency in the perturbed solar wind density (Wind satellite) and geostationary magnetic field (GOES satellite, red line), 2) a peak in PSD is observed at nearly the same frequency at Wind and GOES (blue line), (3) a peak in PSD is observed only at GOES (thick black line), (4) a peak in PSD is observed only at Wind (green line), and (5) no peak is observed (cyan line).

magnetopause displacement (see section 2.2). For comparison, Figure 6 also shows the other wave categories based on the discrete frequency analysis of *Viall et al.* [2009] (see section 2.2): red line is for directly driven waves, dark blue for waves that may be FMR, green line for events without monochromatic ULF waves at 4–5 mHz, and light blue for events without monochromatic wave activity in the solar wind or magnetosphere at 4–5 mHz. Note that this plot is only for one frequency (4–5 mHz) and that these curves may change substantially at other frequencies. The chosen frequency is close to the fundamental FMR frequency in our last two MHD simulations.

Based on Figure 6, the occurrence rate of FMR-like events (black line) does not change with increasing dynamic pressure, unlike the results of *Hartinger et al.* [2013a]. Indeed, none of the curves change substantially with increasing dynamic pressure (the largest change is a reduction in the directly driven wave occurrence rate from roughly 25 to 19%). This observational evidence suggests that FMR occurrence is not affected by magnetopause motion, assuming again that background dynamic pressure can be used as a proxy for magnetopause displacement. This is consistent with the idealized simulations in this study but differs from the results of *Hartinger et al.* [2013a], likely due to the different selection criteria used in *Viall et al.* [2009] and *Hartinger et al.* [2013a]. We return to this point in the next section.

4. Discussion

In the previous section, we examined the effect of magnetopause motion on FMR using global MHD simulations and GOES/Wind satellite observations. Using the three simulations pictured in Figure 1, we obtained the following key results:

1. We demonstrated that BATS-R-US can support FMR in the case of small magnetopause displacements using the same driving conditions as *Claudepierre et al.* [2009].
2. We demonstrated that slow changes to the magnetopause location do not affect the occurrence FMR (though they affect FMR properties).
3. We demonstrated, for the case of a solar wind driver with a broadband frequency spectrum, that the magnetosphere can support FMR over a wide range of typical solar wind conditions.
4. We demonstrated, for the case of a monochromatic solar wind driver, that the magnetosphere can support FMR even for very large and rapid magnetopause displacements.

Using comparisons between the Wind satellite (monitoring solar wind density variations) and the GOES satellite (monitoring predominately compressional magnetic field perturbations at geostationary orbit), we found suggestive evidence that FMR occurrence rates do not change substantially during periods with large dynamic pressure variations and potentially large magnetopause displacements. This is consistent with the simulation results. Thus, during most solar wind conditions, magnetopause displacements do not affect FMR occurrence, though they certainly affect overall ULF wave activity in the dayside magnetosphere.

The MHD simulations in this study were chosen to mimic a wide range of solar wind driving conditions based on realistic scaling between solar wind pressure and pressure perturbations and realistic values for magnetopause displacement speeds and amplitudes [*Takahashi and Ukhorskiy*, 2007; *Plaschke et al.*, 2009]. Our results suggest that, for most conditions, FMR persist in the dayside magnetosphere: the magnetopause normally cannot move fast enough or far enough to prevent FMR occurrence. However, we should use some

©2014. American Geophysical Union. All Rights Reserved.

caution when generalizing these results to all conditions. FMR could still be affected during extreme solar wind, magnetosheath, or ion foreshock conditions which are not well represented by these simulation conditions; these may cause more substantial and rapid magnetopause displacements that significantly affect FMR properties as in the results of *Allan et al.* [1991].

It is also important to note that the magnetospheric magnetic field and plasma density play important roles in determining how sensitive FMR is to magnetopause motion, since it determines T_{FM} and thus sets how fast the magnetopause can move before it affects FMR properties. The Alfvén speed profiles used in these simulations are not representative of all conditions. For example, typical mass densities in our simulation near the magnetopause are roughly 5 amu per cc; this value is typical for quiet conditions but could be significantly larger during active conditions [*Takahashi et al.*, 2010b]. A larger density would affect FMR properties, such as frequency, but we do not think it would significantly alter our results. As shown in Figure 4a and discussed in section 3.1.2, the Alfvén speed profile changes significantly during the simulation due to density increases, yet the FMR was supported throughout the entire simulation.

A more important consideration regarding the mass density is the lack of a well-defined plasmapause in our simulations. If the FMR is confined between the magnetopause and plasmapause, T_{FM} ought to be small compared to the case with an inner boundary inside the nominal plasmapause location. This reduced T_{FM} in turn leads to a reduced sensitivity of FMR occurrence to magnetopause motion, since magnetopause displacements could be regarded as slow compared to T_{FM} (e.g., Figure 1, bottom middle). A reduced cavity size, however, may make FMR occurrence more sensitive to magnetopause displacements that are a larger fraction of the cavity size. These two competing effects will both be more important when the plasmapause is located at a large radial distance (and, thus, the plasmapause/magnetopause cavity is smaller). However, sharp plasmapauses do not tend to occur at large radial distances in the dayside magnetosphere [*Moldwin et al.*, 2002]. Moreover, *Hartinger et al.* [2013a] found peak FMR occurrence inside of 7.5 R_E, suggesting that FMR is not routinely trapped between a plasmapause at a large radial distance and the magnetopause. For these reasons, the lack of a plasmapause does not preclude the use of simulations for dayside FMR, and the main conclusion drawn from the simulations holds: magnetopause motion does not significantly affect FMR occurrence.

If magnetopause motion does not affect FMR occurrence, why did *Hartinger et al.* [2013a] find that FMR occurrence decreases with increasing dynamic pressure/pressure variations, and why have so few FMR been observed in the outer magnetosphere [e.g., *Engebretson et al.*, 1986]? *Kivelson et al.* [1997] suggest that it may be difficult to detect FMR with small amplitudes in the presence of other ULF modes with large amplitudes and similar frequencies. Figure 3 (top) exemplifies this during the latter part of the simulation; large amplitude electric field perturbations with a broadband frequency spectrum obscure the FMR, and the FMR properties only become apparent through additional lines of evidence available in the simulation (e.g., observations from multiple grid cells). This effect likely explains why *Hartinger et al.* [2013a] found reduced FMR occurrence rates during periods with larger dynamic pressure variations; enhancements in non-FMR ULF wave activity caused by the enhanced dynamic pressure fluctuations obscured the FMR. On a related note, *Rickard and Wright* [1995] propose that energy leakage into the magnetotail causes some FMR to have a broadband frequency spectrum, making them more difficult to identify and separate from ambient noise, and *Lee and Lysak* [1991], showed that long duration monochromatic boundary motion near the FMR frequency leads to interference with a broadband frequency spectrum, potentially reducing FMR occurrence rates.

Kivelson et al. [1997] also suggest that ideal conditions are required to observe FMR, such as having multiple satellites at different radial distances; these conditions are only rarely met, potentially leading to lower occurrence rates. This is shown directly by comparing the occurrence rate of global modes found by *Hartinger et al.* [2013a], 1.0%, with the occurrence rate found in this study using the database of *Viall et al.* [2009], ~35%. In both cases, FMR events were required to have monochromatic, compressional magnetic field perturbations, but *Hartinger et al.* [2013a] required several additional criteria based on single and multipoint observations. *Hartinger et al.* [2013a] reported that their occurrence rate for FMR is a lower bound due to the strict identification criteria, the value of ~35% obtained using the database of *Viall et al.* [2009] may include non-FMR wave modes and should thus be regarded as an upper bound. Thus, the chosen identification criteria for FMR affects their occurrence rate, and observational restrictions are a potential reason for the low values reported for FMR occurrence.

©2014. American Geophysical Union. All Rights Reserved.

Low FMR occurrence may also be related to the dependence of fast mode MHD wave propagation on azimuthal wave number. *Lee and Lysak* [1990] and *Lee* [1996] found that fast mode waves with larger azimuthal wave numbers tend to less effectively penetrate from the outer to the inner magnetosphere. If FMR energy sources tend to generate azimuthally structured wave activity, externally driven FMR ought to occur less frequently since the MHD fast mode wave energy would be closely confined to the magnetopause. For example, the ion foreshock can lead to localized magnetopause perturbations and, thus, fast mode waves with larger azimuthal wave numbers than those driven directly by the solar wind [e.g., *Hartinger et al.*, 2013b]. There may only be rare conditions when ion foreshock energy can generate FMR.

5. Summary

In this study, we used a series of idealized global MHD simulations (BATS-R-US) and Wind/GOES satellite observations to examine the effect of magnetopause motion on FMR in the dayside magnetosphere. For the simulations, we considered several types of ULF wave driving conditions: small magnetopause displacements, slow and substantial magnetopause displacements, and large and rapid magnetopause displacements. We used a simulation with small magnetopause displacements to demonstrate that the BATS-R-US simulation code supports FMR, reproducing the LFM simulation results of *Claudepierre et al.* [2009]. We used a simulation with slow and substantial magnetopause displacements to both demonstrate that FMR occurrence is not affected by such displacements and to demonstrate that FMR persist for wide range of typical solar wind driving conditions. We used a simulation with large and rapid magnetopause displacements to show that FMR persist during most conditions; in particular, our results demonstrate that dayside FMR persists for nearly the full range of observed magnetopause displacement amplitudes and speeds [*Plaschke et al.*, 2009]. This conclusion is further supported by Wind and GOES satellite observations, which suggest that FMR occurrence rates do not vary in different magnetopause motion regimes. Thus, although magnetopause motion may affect FMR in extreme cases, the rarity of FMR observations in the outer magnetosphere (i.e., outside the plasmasphere) is due to other factors besides magnetopause motion.

Acknowledgments

We thank S.G. Claudepierre, M. Wiltberger, and M.G. Kivelson for helpful discussions and suggestions. We also thank the NASA Space Science Data facility for use of solar wind data. M.D. Hartinger was funded through NSF grant AGS-1230398. We would like to acknowledge high-performance computing support from Yellowstone (ark:/85065/d7wd3xhc) provided by NCAR's Computational and Information Systems Laboratory, sponsored by the National Science Foundation. We also acknowledge the Extreme Science and Engineering Discovery Environment (XSEDE), which is supported by National Science Foundation grant ACI-1053575. This work was carried out using the SWMF/BATSRUS tools developed at the University of Michigan Center for Space Environment Modeling (CSEM). Simulation output files are available upon request from the corresponding author (M.D. Hartinger, mdhartin@umich.edu). The authors thank Kazue Takahashi and Scott Boardsen for their comments.

Michael Balikhin thanks Kazue Takahashi and Scott Boardsen for their assistance in evaluating this paper.

References

Allan, W., E. M. Poulter, and J. R. Manuel (1991), Magnetospheric cavity modes: Some nonlinear effects, *J. Geophys. Res.*, *96*, 11,461–11,473, doi:10.1029/91JA00657.

Balazs, N. L. (1961), On the solution of the wave equation with moving boundaries, *J. Math Anal. Appl.*, *3*(3), 472–484, doi:10.1016/0022-247X(61)90071-3.

Boris, J. P. (1970), A physically motivated solution of the Alfvén problem, *Tech. Rep. NRL Memorandum Rep., 2167*, Naval Research Laboratory, Washington, D. C.

Claudepierre, S. G., M. Wiltberger, S. R. Elkington, W. Lotko, and M. K. Hudson (2009), Magnetospheric cavity modes driven by solar wind dynamic pressure fluctuations, *Geophys. Res. Lett.*, *36*, L13101, doi:10.1029/2009GL039045.

Elkington, S. R., M. K. Hudson, and A. A. Chan (2003), Resonant acceleration and diffusion of outer zone electrons in an asymmetric geomagnetic field, *J. Geophys. Res.*, *108*(A3), 1116, doi:10.1029/2001JA009202.

Engebretson, M. J., L. J. Zanetti, T. A. Potemra, and M. H. Acuna (1986), Harmonically structured ULF pulsations observed by the AMPTE CCE magnetic field experiment, *Geophys. Res. Lett.*, *13*, 905–908, doi:10.1029/GL013i009p00905.

Gombosi, T. I., G. Tóth, D. L. De Zeeuw, K. C. Hansen, K. Kabin, and K. G. Powell (2002), Semirelativistic magnetohydrodynamics and physics-based convergence acceleration, *J. Comput. Phys.*, *177*, 176–205, doi:10.1006/jcph.2002.7009.

Hartinger, M., V. Angelopoulos, M. B. Moldwin, Y. Nishimura, D. L. Turner, K.-H. Glassmeier, M. G. Kivelson, J. Matzka, and C. Stolle (2012), Observations of a Pc5 global (cavity/waveguide) mode outside the plasmasphere by THEMIS, *J. Geophys. Res.*, *117*, A06202, doi:10.1029/2011JA017266.

Hartinger, M. D., V. Angelopoulos, M. B. Moldwin, K. Takahashi, and L. B. N. Clausen (2013a), Statistical study of global modes outside the plasmasphere, *J. Geophys. Res. Space Physics*, *118*, 804–822, doi:10.1002/jgra.50140.

Hartinger, M. D., D. L. Turner, F. Plaschke, V. Angelopoulos, and H. J. Singer (2013b), The role of transient ion foreshock phenomena in driving Pc5 ULF wave activity, *J. Geophys. Res. Space Physics*, *118*, 299–312, doi:10.1029/2012JA018349.

Hudson, M. K., D. N. Baker, J. Goldstein, B. T. Kress, J. Paral, F. R. Toffoletto, and M. Wiltberger (2014), Simulated magnetopause losses and Van Allen Probe flux dropouts, *Geophys. Res. Lett.*, *41*, 1113–1118, doi:10.1002/2014GL059222.

Jacobs, J. A., Y. Kato, S. Matsushita, and V. A. Troitskaya (1964), Classification of geomagnetic micropulsations, *J. Geophys. Res.*, *69*, 180–181, doi:10.1029/JZ069i001p00180.

Kepko, L., H. E. Spence, and H. J. Singer (2002), ULF waves in the solar wind as direct drivers of magnetospheric pulsations, *Geophys. Res. Lett.*, *29*(8), 1197, doi:10.1029/2001GL014405.

Kivelson, M. G., J. Etcheto, and J. G. Trotignon (1984), Global compressional oscillations of the terrestrial magnetosphere—The evidence and a model, *J. Geophys. Res.*, *89*, 9851–9856, doi:10.1029/JA089iA11p09851.

Kivelson, M., M. Cao, R. McPherron, and R. Walker (1997), A possible signature of magnetic cavity mode oscillations in ISEE spacecraft observations, *J. Geomagn. Geoelec.*, *49*(9), 1079–1098.

Kusse, B., and E. Westwig (1998), *Mathematical Physics: Applied Mathematics for Scientists and Engineers*, John Wiley, New York.

Lee, D.-H. (1996), Dynamics of MHD wave propagation in the low-latitude magnetosphere, *J. Geophys. Res.*, *101*, 15,371–15,386, doi:10.1029/96JA00608.

Lee, D.-H., and R. L. Lysak (1990), Effects of azimuthal asymmetry on ULF waves in the dipole magnetosphere, *Geophys. Res. Lett.*, *17*, 53, doi:10.1029/GL017i001p00053.

©2014. American Geophysical Union. All Rights Reserved.

Lee, D.-H., and R. L. Lysak (1991), Monochromatic ULF wave excitation in the dipole magnetosphere, *J. Geophys. Res.*, *96*(A4), 5811–5817, doi:10.1029/90JA01592.

Lee, D.-H., and R. L. Lysak (1999), MHD waves in a three-dimensional dipolar magnetic field: A search for Pi2 pulsations, *J. Geophys. Res.*, *104*, 28,691–28,700, doi:10.1029/1999JA900377.

Lyon, J. G., J. A. Fedder, and C. M. Mobarry (2004), The Lyon-Fedder-Mobarry (LFM) global MHD magnetospheric simulation code, *J. Atmos. Sol. Terr. Phys.*, *66*, 1333–1350, doi:10.1016/j.jastp.2004.03.020.

Mann, I. R., G. Chisham, and S. D. Bale (1998), Multisatellite and ground-based observations of a tailward propagating Pc5 magnetospheric waveguide mode, *J. Geophys. Res.*, *103*, 4657–4670, doi:10.1029/97JA03175.

Moldwin, M. B., L. Downward, H. K. Rassoul, R. Amin, and R. R. Anderson (2002), A new model of the location of the plasmapause: CRRES results, *J. Geophys. Res.*, *107*(A11), 1339, doi:10.1029/2001JA009211.

Ogilvie, K. W., et al. (1995), SWE, a comprehensive plasma instrument for the wind spacecraft, *Space Sci. Rev.*, *71*, 55–77, doi:10.1007/BF00751326.

Plaschke, F., K.-H. Glassmeier, H. U. Auster, V. Angelopoulos, O. D. Constantinescu, K.-H. Fornaçon, E. Georgescu, W. Magnes, J. P. McFadden, and R. Nakamura (2009), Statistical study of the magnetopause motion: First results from THEMIS, *J. Geophys. Res.*, *114*, A00C10, doi:10.1029/2008JA013423.

Powell, K. G., P. L. Roe, T. J. Linde, T. I. Gombosi, and D. L. De Zeeuw (1999), A solution-adaptive upwind scheme for ideal magnetohydrodynamics, *J. Comput. Phys.*, *154*, 284–209, doi:10.1006/jcph.1999.6299.

Pulkkinen, A., et al. (2013), Community-wide validation of geospace model ground magnetic field perturbation predictions to support model transition to operations, *Space Weather*, *11*, 369–385, doi:10.1002/swe.20056.

Rickard, G. J., and A. N. Wright (1995), ULF pulsations in a magnetospheric waveguide: Comparison of real and simulated satellite data, *J. Geophys. Res.*, *100*, 3531–3537, doi:10.1029/94JA02935.

Ridley, A. J., and M. W. Liemohn (2002), A model-derived storm time asymmetric ring current driven electric field description, *J. Geophys. Res.*, *107*(A8), 1151, doi:10.1029/2001JA000051.

Ridley, A., T. Gombosi, and D. De Zeeuw (2004), Ionospheric control of the magnetosphere: conductance, *Ann. Geophys.*, *22*, 567–584, doi:10.5194/angeo-22-567-2004.

Ridley, A. J., T. I. Gombosi, I. V. Sokolov, G. Tóth, and D. T. Welling (2010), Numerical considerations in simulating the global magnetosphere, *Ann. Geophys.*, *28*, 1589–1614, doi:10.5194/angeo-28-1589-2010.

Samson, J. C., B. G. Harrold, J. M. Ruohoniemi, R. A. Greenwald, and A. D. M. Walker (1992), Field line resonances associated with MHD waveguides in the magnetosphere, *Geophys. Res. Lett.*, *19*, 441–444, doi:10.1029/92GL00116.

Samsonov, A. A., D.-G. Sibeck, and J. Imber (2007), MHD simulation for the interaction of an interplanetary shock with the Earth's magnetosphere, *J. Geophys. Res.*, *112*, A12220, doi:10.1029/2007JA012627.

Samsonov, A. A., D. G. Sibeck, N. V. Zolotova, H. K. Biernat, S. H. Chen, L. Rastaetter, H. J. Singer, and W. Baumjohann (2011), Propagation of a sudden impulse through the magnetosphere initiating magnetospheric Pc5 pulsations, *J. Geophys. Res.*, *116*, A10216, doi:10.1029/2011JA016706.

Singer, H. J., D.-J. Southwood, R. J. Walker, and M. G. Kivelson (1981), Alfven wave resonances in a realistic magnetospheric magnetic field geometry, *J. Geophys. Res.*, *86*, 4589–4596, doi:10.1029/JA086iA06p04589.

Singer, H., L. Matheson, R. Grubb, A. Newman, and D. Bouwer (1996), Monitoring space weather with the GOES magnetometers, in *GOES-8 and Beyond, Society of Photo-Optical Instrumentation Engineers (SPIE) Conference Series*, vol. 2812, edited by E. R. Washwell, pp. 299–308, SPIE Press, Denver, Colo., doi:10.1117/12.254077.

Takahashi, K., and A. Y. Ukhorskiy (2007), Solar wind control of Pc5 pulsation power at geosynchronous orbit, *J. Geophys. Res.*, *112*, A11205, doi:10.1029/2007JA012483.

Takahashi, K., et al. (2010a), Multipoint observation of fast mode waves trapped in the dayside plasmasphere, *J. Geophys. Res.*, *115*, A12247, doi:10.1029/2010JA015956.

Takahashi, K., R. E. Denton, and H. J. Singer (2010b), Solar cycle variation of geosynchronous plasma mass density derived from the frequency of standing Alfvén waves, *J. Geophys. Res.*, *115*, A07207, doi:10.1029/2009JA015243.

Tóth, G., et al. (2005), Space Weather Modeling Framework: A new tool for the space science community, *J. Geophys. Res.*, *110*, A12226, doi:10.1029/2005JA011126.

Troitskaya, V. A., T. A. Plyasova-Bakunina, and A. V. Gul'Elmi (1971), The connection of Pc2-4 pulsations with the interplanetary magnetic field., *Akad. Nauk SSSR Dokl.*, *197*, 1312–1314.

Viall, N. M., L. Kepko, and H. E. Spence (2008), Inherent length-scales of periodic solar wind number density structures, *J. Geophys. Res.*, *113*, A07101, doi:10.1029/2007JA012881.

Viall, N. M., L. Kepko, and H. E. Spence (2009), Relative occurrence rates and connection of discrete frequency oscillations in the solar wind density and dayside magnetosphere, *J. Geophys. Res.*, *114*, A01201, doi:10.1029/2008JA013334.

Waters, C. L., K. Takahashi, D.-H. Lee, and B. J. Anderson (2002), Detection of ultralow-frequency cavity modes using spacecraft data, *J. Geophys. Res.*, *107*(A10), 1284, doi:10.1029/2001JA000224.

Welling, D. T., and A. J. Ridley (2010), Exploring sources of magnetospheric plasma using multispecies MHD, *J. Geophys. Res.*, *115*, A04201, doi:10.1029/2009JA014596.

Yu, Y. Q., and A. J. Ridley (2011), Relative occurrence rates and connection of discrete frequency oscillations in the solar wind density and dayside magnetosphere, *J. Geophys. Res.*, *116*, A04210, doi:10.1029/2010JA015871.

Zhu, X., and M. G. Kivelson (1989), Global mode ULF pulsations in a magnetosphere with a nonmonotonic Alfven velocity profile, *J. Geophys. Res.*, *94*, 1479–1485, doi:10.1029/JA094iA02p01479.

©2014. American Geophysical Union. All Rights Reserved.